

# A reconfigurable silicon photonics chip for the generation of frequency bin entangled qudits

Massimo Borghi,<sup>1,\*</sup> Noemi Tagliavacche,<sup>1</sup> Federico Andrea Sabattoli,<sup>1,†</sup> Houssein El Dirani,<sup>2,‡</sup> Laurene Youssef,<sup>3,§</sup> Camille Petit-Etienne,<sup>3</sup> Erwine Pargon,<sup>3</sup> J.E. Sipe,<sup>4</sup> Marco Liscidini,<sup>1</sup> Corrado Sciancalepore,<sup>2,¶</sup> Matteo Galli,<sup>1,\*\*</sup> and Daniele Bajoni<sup>5</sup>

<sup>1</sup>*Dipartimento di Fisica, Università di Pavia, Via Agostino Bassi 6, Pavia 27100, Italy*

<sup>2</sup>*Université Grenoble Alpes, CEA-Leti, Grenoble cedex 38054, France*

<sup>3</sup>*Univ. Grenoble Alpes, CNRS, CEA/LETI-Minatec, Grenoble INP, LTM, F-38054 Grenoble-France*

<sup>4</sup>*Department of Physics, University of Toronto, 60 St. George Street, Toronto, Ontario M5S 1A7, Canada*

<sup>5</sup>*Dipartimento di Ingegneria Industriale e dell'Informazione,  
Università di Pavia, Via Adolfo Ferrata 5, Pavia 27100, Italy*

(Dated: January 23, 2023)

Quantum optical microcombs in integrated ring resonators generate entangled photon pairs over many spectral modes, and allow the preparation of high dimensional qudit states. Ideally, those sources should be programmable and have a high generation rate, with comb lines tightly spaced for the implementation of efficient qudit gates based on electro-optic frequency mixing. While these requirements cannot all be satisfied by a single resonator device, for which there is a trade-off between high generation rate and tight bin spacing, a promising strategy is the use of multiple resonators, each generating photon pairs in specific frequency bins via spontaneous four-wave mixing.

Based on this approach we present a programmable silicon photonics device for the generation of frequency bin entangled qudits, in which bin spacing, qudit dimension, and bipartite quantum state can be reconfigured on-chip. Using resonators with a radius of  $22\text{ }\mu\text{m}$ , we achieve a high brightness ( $\sim \text{MHz}/(\text{mW})^2$ ) per comb line with a bin spacing of 15 GHz, and fidelities above 85% with maximally entangled Bell states up to a Hilbert space dimension of sixteen. By individually addressing each spectral mode, we realize states that can not be generated on-chip using a single resonator. We measure the correlation matrices of maximally entangled two-qubit and two-qutrit states on a set of mutually unbiased bases, finding fidelities exceeding 98%, and indicating that the source can find application in high-dimensional secure communication protocols.

## I. INTRODUCTION

Increasing the dimensionality of the Hilbert space of any quantum system is important in the development of large scale architectures for quantum technologies. This goal can be achieved either by increasing the number  $n$  of parties involved in the quantum state, or their local dimension  $d$ . For photons, increasing  $d$  presents less challenges than increasing  $n$ . Increasing  $n$  leads to less tolerance to losses, and the lack of strong photon-photon interactions makes the realization of controlled gates very demanding [1]. But multidimensional photon states can be efficiently prepared and controlled by employing one of the many photon degrees of freedom [2], including orbital angular momentum [3], path [4], time [5], and frequency [6], or by using a combination of them [7, 8]. The qudits that can be produced are a greater resource than

the qubits of two-dimensional systems, in that they can be exploited to demonstrate stronger violations of Bell's inequalities [9], they can be used to speed up quantum algorithms [10], and they can reduce circuit depth for logic operations [11]. Their use leads to improved noise resilience in communication protocols [12], and they offer the possibility of deterministically controlling operations between the multiple qubits that can be encoded in the Hilbert space of a single qudit [13].

One of the strategies for the generation of high-dimensional states is to pump a parametric source of photon pairs with a continuous-wave laser; this generates time-frequency entanglement [14, 15]. The large information content per biphoton can be exploited either for transmitting a large alphabet in the time domain [15, 16], or for the deployment of wavelength division multiplexed networks for secure communication [17, 18]. The continuous spectra of photon pairs can be sliced into non-overlapping frequency bins to encode different logical states, an operation that can be effected by filtering the broadband emission with a Fabry-Perot cavity [14]. Alternatively, one can engineer the generation of photons in discrete spectral modes [19].

On integrated platforms, quantum optical Kerr microcombs generated by ring resonators are important sources of high-dimensional frequency entanglement [6, 20–22]. Compared to bulk sources, quantum microcombs have distinctive properties, such as high brightness

\* [massimo.borghi@unipv.it](mailto:massimo.borghi@unipv.it)

† Current address: Advanced Fiber Resources Milan S.r.L, via Fellini 4, 20097 San Donato Milanese (MI), Italy.

‡ Current address: LIGENTEC SA, 224 Bd John Kennedy, 91100 Corbeil-Essonnes, France.

§ Current address: IRCER, Centre Européen de la Céramique, 12 rue Atlantis, 87068 Limoges, France.

¶ Current address: SOITEC SA, Parc Technologique des Fontaines, Chemin des Franques, 38190 Bernin, France.

\*\* [matteo.galli@unipv.it](mailto:matteo.galli@unipv.it)

( $\sim \text{MHz}/(\text{mW})^2$ ), phase coherence over many spectral modes without active stabilization [21], and a free spectral range (FSR) of tens of GHz [20] that allows for the individual address and manipulation of each spectral line [6]. In many applications, this is accomplished through a quantum Fourier processor (QFP), a tool for the coherent manipulation of frequency bin states [23]. It consists of a repeated sequence of electro-optic modulators (EOMs), used for the frequency mixing of the different modes, and waveshapers, employed to apply a different phase shift to each spectral line.

A whole framework of quantum information processing with frequency bins is being developed, leading to a new paradigm for quantum simulation and computation. Arbitrary local operations on qubits have been demonstrated with near unit fidelity and success probability [24–26], and two-qubit gates have been proposed and experimentally realized with both heralded [27] and post selection schemes [28]. A class of local qudit gates, which includes those for the discrete Fourier transform [29] and the frequency hop operation [30], has been demonstrated using the QFP with multi-tone driving of the EOMs. Promisingly, the number of optical elements in a QFP that is required to realize arbitrary qudit gates is predicted to linearly scale with the system size [30].

Crucially, for these operations to be efficient the frequency bin spacing  $\delta$  should not exceed the bandwidth of the EOMs, which is of the order of  $\sim 50$  GHz for commercial devices. If generation is to be done in a single microring resonator, the condition of closely spaced combs requires the use of a ring with a small FSR, and thus a radius of several hundred of microns. This limits its brightness, which scales with the square of the FSR [31]. Recently, it has been shown that this trade-off can be bypassed with the use of multiple resonators, each associated with the generation of a pair of non-degenerate frequency bins [31], and this was demonstrated experimentally for a two qubit system [32, 33]. In that scheme, a single pump is resonant with all the rings, and triggers spontaneous four wave mixing (SFWM) in non-degenerate frequency bins, which occurs because each ring has a different FSR. But this requires the use of auxiliary resonators to ensure that the sources can be pumped both coherently and independently [31].

In this work, we generalize this strategy to demonstrate the generation of programmable frequency-bin-entangled qudits on a silicon photonics chip. We use four identical rings, and offset their comb lines to create equally spaced frequency bins with a separation of  $\delta$ . This quantity can be reconfigured to allow flex-grid (in frequency) operation. Each ring is pumped at a different wavelength with mutually coherent pumps. This configuration allows us to generate entangled states in a Hilbert space up to a dimension of sixteen by using all the four resonators, and does not require the use of auxiliary rings for pump suppression [31, 32].

We first focus on the generation of two-dimensional Bell states, and demonstrate that the source brightness

is independent of the bin spacing. Then we show that the chip can be programmed to generate different qutrit and ququart target states, some of which cannot be directly generated by a single resonator, and we validate their fidelity using quantum state tomography. From the reconstructed density matrices, we certify the qudit dimension through device independent dimension witness [4], and the presence of entanglement from the violation of the generalized Collins-Gisin-Linden-Massar-Popescu (CGLMP) inequalities [9]. Last, with the perspective of implementing our device for secure communication, we measure the correlation matrices of maximally entangled two- and three-dimensional Bell states on a set of mutually unbiased bases. We show fidelities exceeding 98%, comparable to those obtained for path-encoded qudits [4, 34], which certifies the high quality of the generated states and of their coherent control.

## II. RESULTS

Our source consists of a photonic circuit realized on the silicon-on-insulator (SOI) platform; see Supplemental Material [35] for details of the fabrication procedure. The chip is mounted on a sample holder that is temperature stabilized, and metallic microheaters allow us to independently tune different parts of the circuit through the thermo-optic effect. Lensed fibers are used to couple light into and out of the chip through inverse tapers with a coupling loss of approximately 3.5 dB/facet. A sketch of the layout of the device is shown in Fig.1(a). A tree of Mach-Zehnder interferometers (MZ1-MZ3) splits light into four paths, with adjustable amplitudes, and excites four identical add-drop microring resonators (R0-R3) of radius  $22\ \mu\text{m}$  ( $\text{FSR} \simeq 524$  GHz). The comb lines of each pair of rings ( $i, j$ ) are offset by an amount  $\delta_{ij} = \delta|i - j|$ , where  $\delta$  is the tunable bin spacing. The transmission spectra at the output waveguide of the device is shown in Fig.1(c). It displays the four signal and idler resonances that encode the logical states  $|k\rangle_{s(i)}$ , where  $k = 0, 1, 2, 3$ ; here the bin spacing is set to  $\delta = 15$  GHz. The average (loaded) quality factors of the signal and of the idler resonances are respectively  $Q_s \simeq 5.7 \times 10^4$  and  $Q_i \simeq 7.8 \times 10^4$ .

We use four mutually coherent pumps, each resonant with a different ring, to trigger the generation of photon pairs. The pumps are obtained by passing a continuous wave laser ( $\lambda_p = 1551.9$  nm) through a cascade of two electro-optic amplitude modulators (EOAMS), both driven by a sinusoidal radio-frequency (RF) signal at frequency  $\delta$  (see Fig.1(b)). This process creates several sidebands that are equally spaced in frequency. We adjust the relative phase of the two RF signals, and the bias point of the two modulators, to roughly equalize the amplitude of the baseband to that of the first two pairs of sidebands. Four out of the five comb lines are used to pump the rings. Photon pair generation by SFWM occurs in all the rings in a coherent superposition. We operate at a pump power level such that multiple-pair

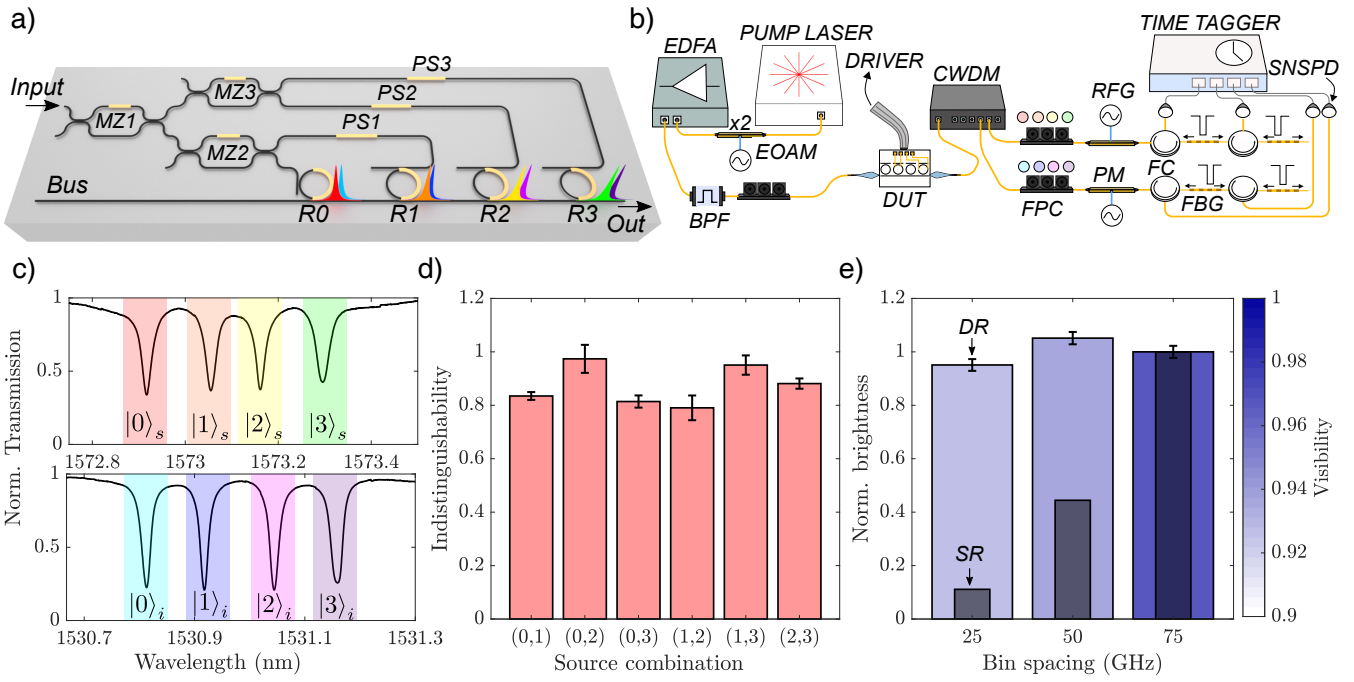


FIG. 1. (a) Sketch of the circuit layout. Light is coupled to the chip from the Input port, and is split by a tree of Mach-Zehnder interferometers (MZ1-MZ3) into four paths, each exciting a microring resonator (R0-R3). The relative phases of the paths can be adjusted using the phase shifters PS1-PS3. Photon pairs are generated by SFWM over different frequency bins (colored pulses indicate a signal-idler pair). (b) Sketch of the experimental setup. EDFA = Erbium-doped fiber amplifier, BPF = bandpass filter, EOAM = electro-optic amplitude modulator, DUT = device under test, CWDM = coarse wavelength division multiplexer, FPC = fiber polarization controller, RFG = radio frequency generator, PM = phase modulator, FC = fiber circulator, FBG = fiber-Bragg-grating, SNSPD = superconducting nanowire single photon detector. (c) Transmission spectra at the output waveguide. Signal and idler photons generated in different frequency bins are labeled as  $|k\rangle_{s(i)}$ , where  $k = [0 - 3]$ . A signal (idler) photon in bin  $k$  can only be generated by the  $k^{\text{th}}$  ring. (d) Indistinguishability between all the possible combinations of sources. (e) Measured brightness of the double (DR) ring source, and simulated brightness of the single (SR) ring source, obtained by varying the frequency bin separation. Values are normalized to that at 75 GHz. The visibility of the two photon interference is mapped into the bar color.

events are negligible, which allows to write the output state as the two-photon state

$$|\Phi\rangle = \frac{1}{\sqrt{D}} \sum_{k=0}^{D-1} \alpha_k |k\rangle_s |k\rangle_i, \quad (1)$$

where  $D$  is the number of frequency bins in the superposition and  $\alpha_k$  are complex coefficients that depend on the pump properties, the MZi and the phase shifters PSi, as shown in Fig. 1(a). Fig. 1(a). Photon pairs are pre-filtered from the pump using a coarse wavelength division multiplexer (CWDM), which also separates the signal from the idler. After that, they pass through separate EO phase modulators (PM), which are used to analyze the state. The PMs are driven by RF signals at a frequency  $\delta$ , which are both coherent with the one driving the EO of the pump. The power  $P_{s(i)}$  and the phase  $\theta_{s(i)}$  of the signal (idler) PM is varied in the state analysis. Tunable wavelength fiber-Bragg-gratings (FBG), with a bandwidth of 10 GHz, are used to filter out photons from specific combinations of frequency bins, which are then detected by an array of superconducting nanowire single-

photon detectors (SNSPDs). Coincidence measurements between the arrival time of the signal and the idler photon are performed using a time-tagging electronics. We used four FBGs and four detectors to simultaneously measure four different frequency bin combinations for each filter setting, which reduces the characterization time significantly.

### A. Sources indistinguishability and flex-grid operation

The two-photon state in Eq.(1) consists in a coherent superposition of  $D$  frequency bins, each associated with a different source. And each has a different joint spectral amplitude  $\Phi_i(\omega_s, \omega_i)$ , which describes the intra-bin frequency correlation between signal and idler photons. However, those fine-grain correlations are neglected in the simpler description (1) of the state, in which the frequency distribution is collapsed to a single label  $|k\rangle_s |k\rangle_i$ . It can be demonstrated that this simplified model reproduces the measurement outcomes if the elements  $\rho_{jj,kk}$  of

the density matrix  $\rho = |\Phi\rangle\langle\Phi|$  are replaced by  $\rho_{jj,kk} \rightarrow I_{jk}\rho_{jj,kk}$ , where  $I_{jk}$  is the indistinguishability between source  $i$  and  $j$  (see Supplemental Material [35] for details). For  $I_{jk} < 1$ , the modified density matrix describes a mixed state, as the fine-grain correlations depends on the specific bin. Thus the  $I_{jk}$  are key parameters to characterize the state. The fine-grain indistinguishability can be measured by equally pumping two rings, say  $j$  and  $k$ , to generate the maximally entangled two-qubit state  $|\psi\rangle = (|j\rangle_s|j\rangle_i + |k\rangle_s|k\rangle_i)/\sqrt{2}$ , and by recording a two-photon interference fringe from the projection of the signal and the idler photon on  $\langle j|_{s(i)} + e^{j\theta_{s(i)}}\langle k|_{s(i)}$ ;  $I_{jk}$  can be extracted from the visibility  $V_{jk}$  of the fringe, where for a qubit  $V_{jk} = I_{jk}$  [6].

For this experiment, the bin spacing are set to 15 GHz. The signal/idler projectors are realized by adjusting the RF power driving the PMs to equalize the intensity  $|J_{\pm 1}|$  of the first-order sidebands to that of the baseband ( $|J_0|$ ); here the  $J_n$  are Bessel functions of the first kind, with their argument equal to the strength of the modulation index (see Supplemental Material [35]). The RF phase  $\theta_s = \theta_i = \bar{\theta}$  is varied to record a two-photon interference coincidence measurement, in which the count rate is proportional to  $\propto 1 + V\cos(2\theta)$  [6, 20]. The measured values of  $I_{jk}$  are reported in Fig.1(d). The indistinguishability values are within the interval  $[0.8 - 1]$ , with an average value of  $V = 0.87(7)$ . This means that the joint spectral amplitudes of the different sources do not perfectly overlap. This is not surprising, for the resonances of the four resonators slightly differ in both their quality factors and extinctions, most likely due to small inhomogeneities in the waveguide-resonator coupling gap (almost at the very limit of the lithographic tool).

We now turn to the brightness of each resonator, which has an average value of  $B = (0.63 \pm 0.15)\text{MHz}/(\text{mW})^2$ . Unlike the case of a single ring [31], in our system the brightness does not depend on the choice of the bin spacing. For example, we consider the Bell state  $|\psi\rangle$  generated by pumping resonators R2 and R3 and measure the sum of the brightness of the two sources for three different bin spacing  $\delta$ : 25 GHz, 50 GHz and 75 GHz. The results, shown in Fig.1(e), are normalized to the brightness level measured at a bin separation of 75 GHz. For each configuration, we also calculated the brightness of a single ring with  $\text{FSR}=\delta$  and with the same Q-factor. The data for a single ring are normalized to the brightness level calculated at a bin separation of 75 GHz. For the double ring structure, the variation of the brightness between the different configurations is negligible. Instead, if a single ring were used, there would be a reduction of almost one order of magnitude between the smallest and the largest bin separation ( $(25/75)^2 \simeq 0.11$ ), due to the intrinsic trade-off between brightness and ring finesse [31]. Note that a bin spacing of 15 GHz in a single ring with the same Q-factor would correspond to a generation rate  $(15/524)^2 \sim 10^{-3}$  times smaller than that of a double ring source. Moreover, the single ring would have a radius  $R = (v_g/(2\pi\delta)) \sim 800\ \mu\text{m}$ , where  $v_g$  is the group

velocity, occupying a footprint  $\sim 10^3$  times larger than that of the four rings.

The bin spacing can be reconfigured (flex-grid operation) without compromising the quality of entanglement. We prove this by extracting the visibility of quantum interference for each bin spacing; under the assumption of the presence of a color-less noise in our system, this can be used to certify entanglement [9]. Following the approach of Imany et al. [20], we set the driving frequency of the PMs to be half of the bin spacing and collect coincidences in the bins half-way between  $|2\rangle_{s(i)}$  and  $|3\rangle_{s(i)}$ . The fringe visibilities  $V$  are reported in Fig.1(e). These are all above 95%, and they do not depend on the bin separation. Moreover, being greater than  $1/\sqrt{2}$ , they also indicate entanglement in the generated state [6].

## B. Programmable generation of qudit states

We now demonstrate the programmability of our device by generating a variety of entangled qudit states that we characterize through quantum state tomography. In what follows, the bin spacing is fixed to 15 GHz. Quantum state tomography is performed with  $N$  measurement settings  $\mathcal{M}(\gamma) = \{\mathcal{M}_i(\gamma_i)\}_{i=1,\dots,N}$ , each associated with a set of  $D^2$  positive operator-valued measures (POVM)  $\{\mathcal{P}_{iq}\}_{q=1,\dots,D^2}$  that describe all the possible experimental measurement outcomes, where the probability of obtaining the  $q^{\text{th}}$  outcome for the  $i^{\text{th}}$  measurement setting is  $\text{Tr}(\rho\mathcal{P}_{iq})$ . We use  $\gamma_i$  to indicate the  $i^{\text{th}}$  measurement setting (RF power and phase) of the signal and the idler PM. The POVMs  $\mathcal{P}_{iq}$  are defined as  $\mathcal{P}_{iq} = U^\dagger(\gamma_i)|q\rangle\langle q|U(\gamma_i)$ , where  $U(\gamma_i)$  describes the action of the PMs on the system and  $|q\rangle$  indicates one of the  $D^2$  computational basis vectors. We used  $N = 5$  measurement settings for  $D = 2$ , and  $N = 17$  for  $D = 3$  and  $D = 4$ , corresponding respectively to 20 ( $D = 2$ ), 153 ( $D = 3$ ) and 272 ( $D = 4$ ) POVMs. These are more than the  $D^4$  measurements required to unambiguously determine the density matrix, but the redundancy helps to speed up the convergence of the reconstruction algorithm (maximum likelihood). The complete list of the  $\gamma_i$  is reported in the Supplemental Material [35].

We first program the two-qubit Bell state  $|\Phi_1\rangle = (|22\rangle + |33\rangle)/\sqrt{2}$  by coherently pumping rings R2 and R3. The reconstructed density matrix  $\rho_r$  is shown in Fig.2(a). The state purity is  $\mathcal{P}_1 = 94.63(4)\%$  and the fidelity  $\mathcal{F}_1 = \text{Tr}\sqrt{\sqrt{\rho_t}\rho_r\sqrt{\rho_t}}$  with respect to the target density matrix  $\rho_t = |\Phi_1\rangle\langle\Phi_1|$  is 95.0(2)%.

We then program the device to generate the two qutrit states  $|\Phi_2\rangle = (|11\rangle + |22\rangle + |33\rangle)/\sqrt{3}$  and  $|\Phi_3\rangle = (|11\rangle - |22\rangle - |33\rangle)/\sqrt{3}$ . Note that  $|\Phi_3\rangle$  cannot be directly generated using a single ring resonator without a subsequent state manipulation, for example by using a waveshaper. On the contrary, in our device, the state can be built “piece by piece” by controlling the contributions of each generating ring. Indeed, the states  $|\Phi_2\rangle$  and  $|\Phi_3\rangle$  are obtained by coherently pumping the rings R1, R2, and

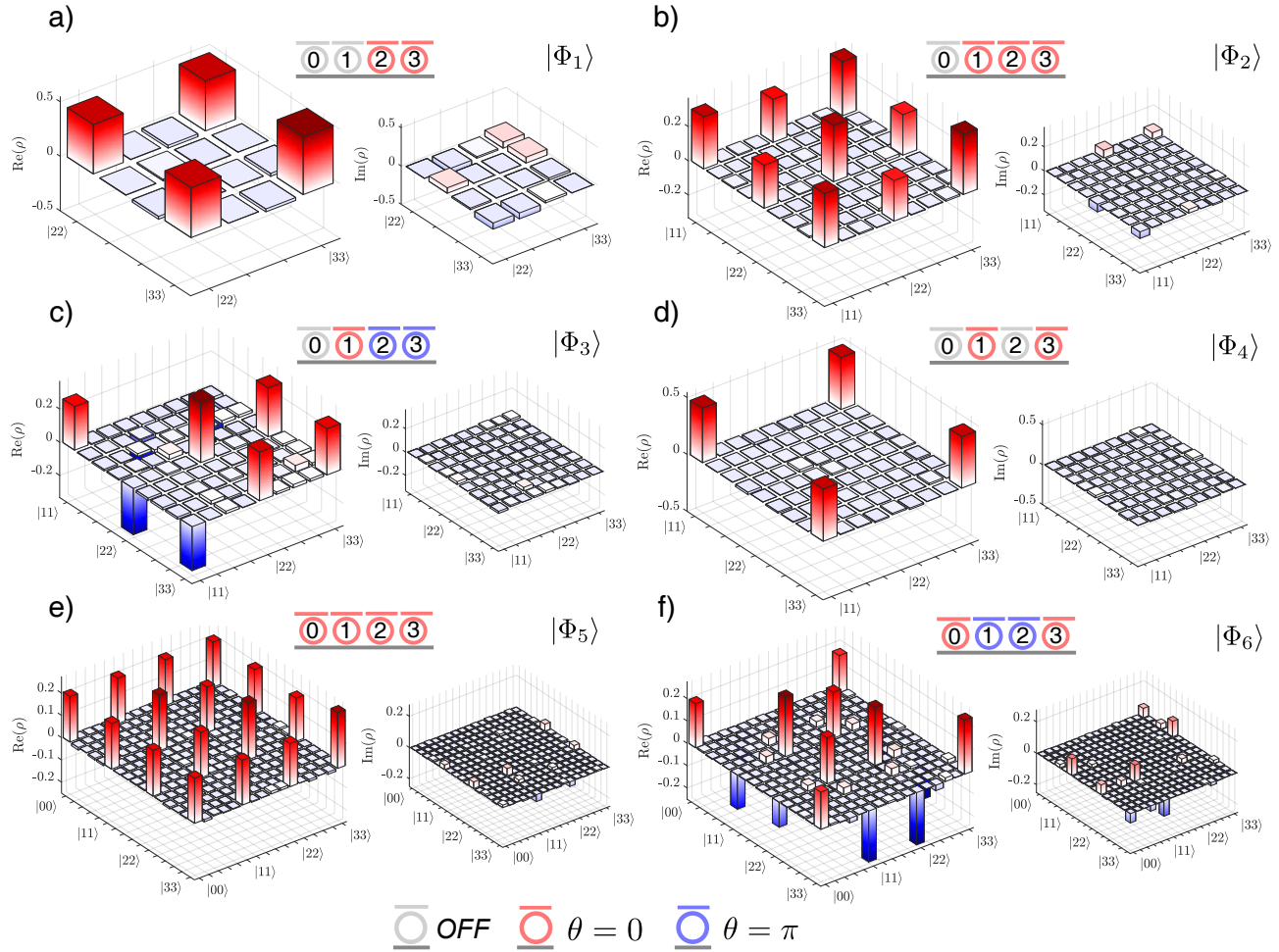


FIG. 2. (a-f): Reconstructed density matrices (the real and the imaginary parts are reported respectively to the left and to the right of each panel) for the different target quantum states reported in Table I. The sketch on the top of each matrix indicates the status of the four rings R0-R3 (the gray color corresponds to an off-resonance source) and the phase of each term in the quantum states in Table I.

R3. For  $|\Phi_2\rangle$ , the relative phases between the biphoton emissions from all the sources are set equal, while for  $|\Phi_3\rangle$  the emission from source 1 is set to have a phase shift of  $\pi$  with respect to those of sources 2 and 3. The phases are regulated through the on-chip phase shifters PS1 and PS2 in Fig.1(a). More details on the calibration procedure are given in the Supplemental Material [35].

The reconstructed density matrices are shown in Fig.2(b-c). The fidelity with the target states  $|\Phi_2\rangle$  and  $|\Phi_3\rangle$  are respectively  $\mathcal{F}_2 = 86.2(3)$  and  $\mathcal{F}_3 = 86.1(3)$ , while the purities are respectively  $\mathcal{P}_2 = 78.3(5)$  and  $\mathcal{P}_3 = 79.3(5)$ , and are limited by the indistinguishability  $I_{jk}$  between the sources. Indeed, if one considers an average value of  $0.87(7)$  for  $I_{jk}$ , which is the result shown in Fig.1(d), our simulations indicate that the maximum attainable fidelity and purity for both states are  $\mathcal{F}_{\max} = 91(5)\%$  and  $\mathcal{P}_{\max} = 84(8)\%$  respectively; see Supplemental Material [35]. In addition, we believe that low purity values might be due to an imperfect calibration of the PMs and to drifts of the system during the

data acquisition.

The programmability of our source can be exploited to dynamically change the number of terms in the Bell state that is being generated. As an example, we first programmed the device to output the state  $|\Phi_2\rangle$ , and then we implemented the transformation  $|\Phi_2\rangle \rightarrow |\Phi_4\rangle$ , where  $|\Phi_4\rangle = (|11\rangle + |33\rangle)/\sqrt{2}$ , by detuning R2 from the resonance condition. To reconstruct the density matrix of this state, we used the same measurement settings implemented for  $|\Phi_2\rangle$ , which allows us to evaluate the magnitude of residual component of the state  $|22\rangle$  in  $|\Phi_4\rangle$ . The reconstructed density matrix is reported in Fig.2(d), showing a fidelity of  $\mathcal{F}_4 = 93.2(2)\%$  with the target state, and a purity of  $\mathcal{P}_4 = 88.5(4)\%$ . The elements  $\rho_{22,jj}$  are comparable to the noise floor.

As a last example, we programmed the device to generate the two-ququart entangled states  $|\Phi_5\rangle = (|00\rangle + |11\rangle + |22\rangle + |33\rangle)/\sqrt{4}$  and  $|\Phi_6\rangle = (|00\rangle - |11\rangle - |22\rangle + |33\rangle)/\sqrt{4}$ ; note that the state  $|\Phi_6\rangle$  cannot be generated by a single resonator. The two-ququart states are obtained by

pumping all four rings R0-R3 simultaneously, and by regulating the relative phase of their biphoton emission using the phase shifters PS1, PS2, and PS3 in Fig.1(a). The reconstructed density matrices are reported in Fig.2(e-f). We computed a fidelity of  $\mathcal{F}_5 = 84.5(2)\%$  for  $|\Phi_5\rangle$ , and  $\mathcal{F}_6 = 79.0(1)\%$  for  $|\Phi_6\rangle$ , with purities of respectively  $\mathcal{P}_5 = 74.4(4)\%$  and  $\mathcal{P}_6 = 76.2(1)\%$ .

Finally, we used the reconstructed density matrices to confirm that the generated states violate the generalized CGLMP inequality for qudits [9], which verifies the presence of entanglement. The calculated CGLMP parameter  $S$  is reported in Table I. For all the states we find that  $S > 2$ , hallmarking the presence of non-local correlations. One can also investigate the local qudit dimension through device independent dimension witness. As explained by Wang et al. [4], it is possible to calculate a lower bound  $[\mathcal{D}]$  (where  $[x]$  indicates the least integer greater than  $x$ ) of the dimensionality of each subsystem from only local measurements in the  $Z$ -basis (i.e., the computational basis). Following this approach, we computed the values of  $\mathcal{D}$  shown in Table I, which certify a local dimension of  $[\mathcal{D}] = 2$  for  $|\Phi_{1,4}\rangle$ ,  $[\mathcal{D}] = 3$  for  $|\Phi_{2,3}\rangle$ , and  $[\mathcal{D}] = 4$  for  $|\Phi_{5,6}\rangle$ .

Label $\{\alpha_0, \alpha_1, \alpha_2, \alpha_3\}$	Fidelity	Purity	CGLMP	$\mathcal{D}$
$ \Phi_1\rangle \{0, 0, 1, 1\}$	95.0(2)	94.63(4)	2.59(1)	1.882(5)
$ \Phi_2\rangle \{0, 1, 1, 1\}$	86.2(3)	78.3(5)	2.37(1)	2.948(2)
$ \Phi_3\rangle \{0, 1, -1, -1\}$	86.1(3)	79.3(5)	2.337(7)	2.705(5)
$ \Phi_4\rangle \{0, 1, 0, 1\}$	93.2(2)	88.5(4)	2.74(1)	1.947(2)
$ \Phi_5\rangle \{1, 1, 1, 1\}$	84.5(2)	74.4(4)	2.336(7)	3.747(5)
$ \Phi_6\rangle \{1, -1, -1, 1\}$	79.0(1)	76.2(1)	2.066(4)	3.883(4)

TABLE I. Values of the fidelity, purity, CGLMP parameter and dimension witness  $\mathcal{D}$  for the target states  $\Phi_j$  ( $j = [1 - 6]$ ). Each state is defined by the list of coefficients  $\alpha_k$  as  $\frac{1}{\sqrt{D}} \sum_{k=0}^{D-1} \alpha_k |kk\rangle$ . Errors are computed by assuming a Poissonian statistics on the recorded coincidences.

### C. Qubit and qutrit correlations on mutually unbiased basis

Given two orthonormal basis sets  $\{|e_1\rangle, \dots, |e_D\rangle\}$  and  $\{|f_1\rangle, \dots, |f_D\rangle\}$ , these are said to be mutually unbiased if  $\langle e_j | f_k \rangle = D^{-1}$ . The generation of entangled states and the ability of two users to perform projections on a set of mutually unbiased basis are the backbone of many secure communication protocols [12]. Maximally entangled Bell states have the property that the outcomes of the measurements between two parties, say Alice and Bob, are always perfectly correlated or anti-correlated when they measure by using the same basis. This allows users to share the same secret key in a communication protocol. At the same time, the two outcomes are completely uncorrelated when Alice and Bob choose two mutually unbiased basis sets. More formally, given a maximally entangled Bell state  $|\Phi\rangle$ , we have that  $|\langle e_j e_k^* | \Phi \rangle|^2 = D^{-1} \delta_{jk}$  and  $|\langle e_j f_k^* | \Phi \rangle|^2 = D^{-1}$ , where the states  $|f^*\rangle, |e^*\rangle$  are

obtained from the complex conjugation of the expansion coefficients of  $|f\rangle, |e\rangle$  on the computational basis. An important parameter that allows one to predict an upper bound to the tolerable level of errors in the communication, and which defines the amount of secure bits that can be extracted from the secret key, is the fidelity  $\mathcal{F}_{\text{mub}}$  with which such correlations are reproduced in the experiment [12, 34].

We evaluate this parameter for our entangled photon source by using the PMs to perform projective measurements on mutually unbiased basis. We choose to work with the qubit and qutrit states  $|\Phi_1\rangle$  and  $|\Phi_2\rangle$ . For the qubit, we choose the eigenvectors of the Pauli operators  $X$ ,  $Y$ , and  $Z$  as a set of three mutually unbiased basis. The projections on the  $X$  and  $Y$  basis are implemented by first adjusting the RF power of the PMs to have  $|J_0| = |J_{\pm 1}| = \bar{J}$ , and then by choosing the RF phases within the set  $\{0, \pi\}$  ( $X$  set) or  $\{0, \pi/2\}$  ( $Y$  set). We collect coincidences from the signal/idler bins  $|2\rangle$ . In the case of the qutrit, we only implement two out of the four mutually unbiased basis sets [36], which we choose to be the  $Z$  and the Fourier basis [4]. The remaining sets cannot be implemented with a single PM, since they require photon projection on bin superpositions that have a relative phase that is not monotonic with the bin number [36]. However, they could be realized with a QFP [29]. The Fourier basis is realized by setting the PMs to have  $|J_0| = |J_{\pm 1}|$ , and then by varying the RF phases within the set  $\{0, 2\pi/3, 4\pi/3\}$ . Coincidences are collected in the signal/idler bin  $|1\rangle$ . Because  $J_{-n} = (-1)^n J_n$ , we actually implement  $I^- F$ , where  $I^-$  is a  $3 \times 3$  identity matrix except that  $I_{33}^- = -1$ , and  $F$  is the Fourier matrix [27]. The measured correlation matrices  $C_e$  for dimension  $D = 2$  (qubit) and  $D = 3$  (qutrit) are respectively shown in Fig.3(a) and in Fig.3(b). The fidelity  $\mathcal{F}_{\text{mub}}$  with the theoretical expectations  $C_t$  is defined as [30]

$$\mathcal{F}_{\text{mub}} \equiv \frac{\text{Tr}(C_e^\dagger C_t) \text{Tr}(C_t^\dagger C_e)}{\text{Tr}(C_e^\dagger C_e) \text{Tr}(C_t^\dagger C_t)}. \quad (2)$$

We find  $\mathcal{F}_{\text{mub}} = 98.76(3)\%$  for  $D = 2$ , and  $\mathcal{F}_{\text{mub}} = 98.78(3)\%$  for  $D = 3$ , which are values comparable to those obtained for path-encoded qudits [4, 34].

As shown in Fig.3, the probabilities of the outcomes associated with the superposition basis  $X$ ,  $Y$  and  $F$  do not sum to one. This happens because the PMs also scatter photons outside the computational basis, so that the implemented projectors  $|e'\rangle = \bar{J} \sqrt{D} |e\rangle$  (where  $|e\rangle$  can be any of the eigenvectors of the operators  $X$ ,  $Y$  or  $F$ ) are not normalized to one. This does not introduce any bias in the correlation matrices in Fig.3, and it acts only as an excess loss.

More generally, the transformation imparted by a PM is described by a circulant matrix  $W$  defined on the infinite-dimensional space spanned by equidistant frequency bins [30]. Consequently, if  $W$  changes the measurement basis to  $Q = \{|q_0\rangle, \dots, |q_{D-1}\rangle\} = \{W^\dagger |0\rangle, \dots, W^\dagger |D-1\rangle\}$ , the coefficients  $W_{ik}$  of the expansion  $|q_i\rangle = \sum_k W_{ik} |i\rangle$  are related by  $W_{ik} =$

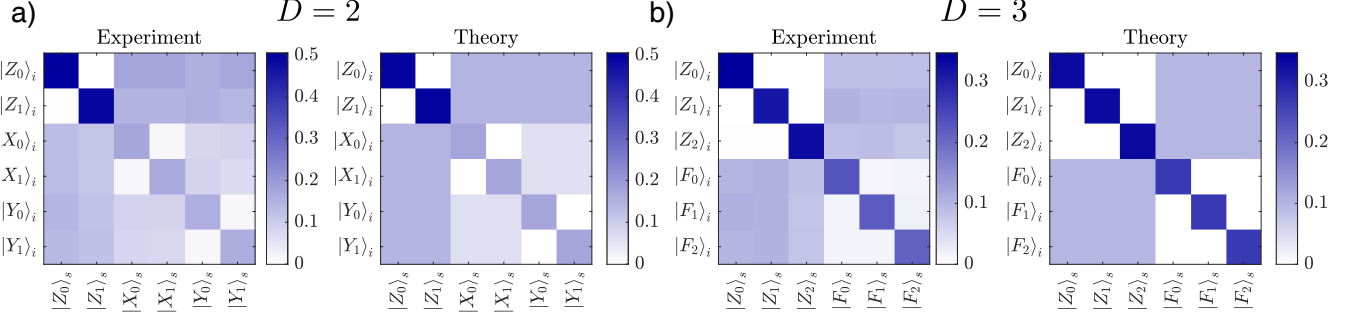


FIG. 3. (a) Experimental (left panel) and theoretical (right panel) distribution of the outcomes associated with the projections of the Bell state  $|\Phi_1\rangle$  on a set of three mutually unbiased basis. These are the eigenvectors of the Pauli  $X$ ,  $Y$  and  $Z$  operators. (b) Same as in panel (a), but relative to the three-dimensional Bell state  $|\Phi_2\rangle$ . The two sets of mutually unbiased basis are the eigenvectors of the Pauli  $Z$  operator and the Fourier basis  $F$ .

$W_{i+m, k+m}$  (where  $m$  is an integer number). Within the three-dimensional space  $\text{span}\{|0\rangle, |1\rangle, |2\rangle\}$ , the PM can implement the transformation  $W^\dagger |1\rangle = J_{-1} |0\rangle + J_0 |1\rangle + J_1 |2\rangle = \bar{J}\sqrt{3} |F_0\rangle$  ( $|F_0\rangle = (|0\rangle + |1\rangle - |2\rangle)/\sqrt{3}$ ), which allows us to estimate the probability  $\langle F'_0 | \rho | F'_0 \rangle$  from the photon counts measured on  $|1\rangle$ , but the same PM setting will also implement  $W^\dagger |0\rangle = J_0 |0\rangle + J_1 |1\rangle + J_2 |2\rangle$  and  $W^\dagger |2\rangle = J_{-2} |0\rangle + J_{-1} |1\rangle + J_0 |2\rangle$ , which differ with respect to both  $|F_1\rangle = (e^{-i\frac{2\pi}{3}} |0\rangle + |1\rangle - e^{i\frac{2\pi}{3}} |2\rangle)/\sqrt{3}$  and  $|F_2\rangle = (e^{-i\frac{4\pi}{3}} |0\rangle + |1\rangle - e^{i\frac{4\pi}{3}} |2\rangle)/\sqrt{3}$  (e.g.,  $J_{-2}$  cannot be equal to  $J_{-1}$  and  $J_0$  simultaneously). As a consequence, we can apply  $W$  to map any of the (not normalized) vectors  $|F'_j\rangle = \bar{J}\sqrt{D} |F_j\rangle$  to a particular  $Z$ -basis vector, in this case  $|1\rangle$ , but  $W$  will not map  $|F'_{j \neq k}\rangle$  to  $|0\rangle$  and  $|2\rangle$ ; these basis vectors can not be measured without changing the PM setting. It will be then very inefficient to run a communication protocol using only PMs, but these limitations can be overcome through the use of QFPs, which can be used to implement arbitrary qubit gates [24] and the high-dimensional Fourier gate [29] with almost unit probability. The process fidelity of those gates exceeds 99.9%, which suggests that high-dimensional entanglement-based QKD could be implemented by using our source.

### III. CONCLUSION

We presented a programmable silicon photonics chip for the generation of frequency-bin entangled qudits up to a dimension of four. Each bin is associated with the spontaneous emission of photon pairs from different high-finesse ring-resonators, thus decoupling the generation rate from the spectral separation of the bins. The device can be programmed to generate multiple qudit entangled states, including some that cannot be directly generated using a single ring. All the generated states were validated by quantum state tomography. We measured the correlation matrices of maximally entangled two-qubit

and two-qutrit states when projected on different mutually unbiased basis sets, finding a high fidelity with the target correlation matrices. This indicates that our source could be used in high dimensional secure communication protocols, and we can envision other applications, such as the multiplexing of single photons.

Indeed, a variable electro-optic frequency shift can be used as a feed-forward operation to increase the probability of having a single photon at the output without a corresponding increase of multiphoton events [37]. A similar approach has been used to herald single photons in pure spectral modes [38]. In both cases, the number of multiplexed spectral modes is limited by the maximum frequency shift that can be imparted to the photons. It is then important to have a source that generates closely spaced and bright spectral modes, which are exactly what our device can provide.

Furthermore, we could exploit the programmability of our source in quantum simulations and multiphoton interference. For example, quantum transport of correlated biphotons in discrete frequency modes exhibits a rich variety of behaviors, from walks showing enhanced ballistic transport to subspaces featuring scattering centers or local traps [39]. Interestingly, one can change from a diffusion regime to another by modifying the relative phases between the comb lines, which in our case can be done on chip. Since the walk-depth increases with the strength of the electro-optic modulation, large depths could be reached by using comb lines that are closely spaced, for which the electro-optic mixing is more effective. Very generally, the high brightness of our source could be exploited to probe multiphoton interference in the frequency domain, in analogy with boson sampling experiments previously reported in path [40] and time-bin encoding [41], or in frustrated interference [42, 43].

### ACKNOWLEDGMENTS

This work has been supported by Ministero dell’Istruzione, dell’Università e della Ricerca

[MIUR grant Dipartimenti di Eccellenza 2018-2022 (F11I18000680001)]. This work is partly supported by the French RENATECH network. J. E. S. acknowledges support from the Natural Sciences and Engineering Re-

search Council of Canada. The device has been designed using the open source Nazca design<sup>TM</sup> framework.

---

[1] E. Knill, R. Laflamme, and G. J. Milburn, A scheme for efficient quantum computation with linear optics, *Nature* **409**, 46 (2001).

[2] M. Erhard, M. Krenn, and A. Zeilinger, Advances in high-dimensional quantum entanglement, *Nat. Rev. Phys.* **2**, 365 (2020).

[3] M. Zahidy, Y. Liu, D. Cozzolino, Y. Ding, T. Morioka, L. K. Oxenløwe, and D. Bacco, Photonic integrated chip enabling orbital angular momentum multiplexing for quantum communication, *Nanophotonics* **11**, 821 (2022).

[4] J. Wang, S. Paesani, Y. Ding, R. Santagati, P. Skrzypczyk, A. Salavrakos, J. Tura, R. Augusiak, L. Mančinska, D. Bacco, *et al.*, Multidimensional quantum entanglement with large-scale integrated optics, *Science* **360**, 285 (2018).

[5] N. T. Islam, C. C. W. Lim, C. Cahall, J. Kim, and D. J. Gauthier, Provably secure and high-rate quantum key distribution with time-bin qudits, *Sci. Adv.* **3**, e1701491 (2017).

[6] M. Kues, C. Reimer, P. Roztocki, L. R. Cortés, S. Sciara, B. Wetzel, Y. Zhang, A. Cino, S. T. Chu, B. E. Little, *et al.*, On-chip generation of high-dimensional entangled quantum states and their coherent control, *Nature* **546**, 622 (2017).

[7] P. Imany, J. A. Jaramillo-Villegas, M. S. Alshaykh, J. M. Lukens, O. D. Odele, A. J. Moore, D. E. Leaird, M. Qi, and A. M. Weiner, High-dimensional optical quantum logic in large operational spaces, *Npj Quantum Inf.* **5**, 1 (2019).

[8] H.-H. Lu, Z. Hu, M. S. Alshaykh, A. J. Moore, Y. Wang, P. Imany, A. M. Weiner, and S. Kais, Quantum phase estimation with time-frequency qudits in a single photon, *Adv. Quantum Technol.* **3**, 1900074 (2020).

[9] D. Collins, N. Gisin, N. Linden, S. Massar, and S. Popescu, Bell inequalities for arbitrarily high-dimensional systems, *Phys. Rev. Lett.* **88**, 040404 (2002).

[10] Y. Wang, Z. Hu, B. C. Sanders, and S. Kais, Qudits and high-dimensional quantum computing, *Front. Phys.* **8**, 589504 (2020).

[11] B. P. Lanyon, M. Barbieri, M. P. Almeida, T. Jennewein, T. C. Ralph, K. J. Resch, G. J. Pryde, J. L. O'brien, A. Gilchrist, and A. G. White, Simplifying quantum logic using higher-dimensional hilbert spaces, *Nat. Phys.* **5**, 134 (2009).

[12] N. J. Cerf, M. Bourennane, A. Karlsson, and N. Gisin, Security of quantum key distribution using d-level systems, *Phys. Rev. Lett.* **88**, 127902 (2002).

[13] C. Vigliar, S. Paesani, Y. Ding, J. C. Adcock, J. Wang, S. Morley-Short, D. Bacco, L. K. Oxenløwe, M. G. Thompson, J. G. Rarity, *et al.*, Error-protected qubits in a silicon photonic chip, *Nat. Phys.* **17**, 1137 (2021).

[14] K.-C. Chang, X. Cheng, M. C. Saruhan, A. K. Vinod, Y. S. Lee, T. Zhong, Y.-X. Gong, Z. Xie, J. H. Shapiro, F. N. Wong, *et al.*, 648 hilbert-space dimensionality in a biphoton frequency comb: entanglement of formation and schmidt mode decomposition, *Npj Quantum Inf.* **7**, 1 (2021).

[15] X. Liu, X. Yao, H. Wang, H. Li, Z. Wang, L. You, Y. Huang, and W. Zhang, Energy-time entanglement-based dispersive optics quantum key distribution over optical fibers of 20 km, *Appl. Phys. Lett.* **114**, 141104 (2019).

[16] I. Ali-Khan, C. J. Broadbent, and J. C. Howell, Large-alphabet quantum key distribution using energy-time entangled bipartite states, *Phys. Rev. Lett.* **98**, 060503 (2007).

[17] X. Liu, X. Yao, R. Xue, H. Wang, H. Li, Z. Wang, L. You, X. Feng, F. Liu, K. Cui, *et al.*, An entanglement-based quantum network based on symmetric dispersive optics quantum key distribution, *APL Photonics* **5**, 076104 (2020).

[18] S. K. Joshi, D. Aktas, S. Wengerowsky, M. Lončarić, S. P. Neumann, B. Liu, T. Scheidl, G. C. Lorenzo, Ž. Samec, L. Kling, *et al.*, A trusted node-free eight-user metropolitan quantum communication network, *Sci. Adv.* **6**, eaaba0959 (2020).

[19] C. L. Morrison, F. Graffitti, P. Barrow, A. Pickston, J. Ho, and A. Fedrizzi, Frequency-bin entanglement from domain-engineered down-conversion, *APL Photonics* **7**, 066102 (2022).

[20] P. Imany, J. A. Jaramillo-Villegas, O. D. Odele, K. Han, D. E. Leaird, J. M. Lukens, P. Lougovski, M. Qi, and A. M. Weiner, 50-ghz-spaced comb of high-dimensional frequency-bin entangled photons from an on-chip silicon nitride microresonator, *Opt. Express* **26**, 1825 (2018).

[21] J. A. Jaramillo-Villegas, P. Imany, O. D. Odele, D. E. Leaird, Z.-Y. Ou, M. Qi, and A. M. Weiner, Persistent energy-time entanglement covering multiple resonances of an on-chip biphoton frequency comb, *Optica* **4**, 655 (2017).

[22] H.-H. Lu, K. V. Mylswamy, R. S. Bennink, S. Seshadri, M. S. Alshaykh, J. Liu, T. J. Kippenberg, D. E. Leaird, A. M. Weiner, and J. M. Lukens, Bayesian tomography of high-dimensional on-chip biphoton frequency combs with randomized measurements, *Nat. Commun.* **13**, 1 (2022).

[23] H.-H. Lu, J. M. Lukens, N. A. Peters, B. P. Williams, A. M. Weiner, and P. Lougovski, Quantum interference and correlation control of frequency-bin qubits, *Optica* **5**, 1455 (2018).

[24] H.-H. Lu, E. M. Simmernan, P. Lougovski, A. M. Weiner, and J. M. Lukens, Fully arbitrary control of frequency-bin qubits, *Phys. Rev. Lett.* **125**, 120503 (2020).

[25] H.-H. Lu, J. M. Lukens, N. A. Peters, O. D. Odele, D. E. Leaird, A. M. Weiner, and P. Lougovski, Electro-optic frequency beam splitters and tritters for high-fidelity photonic quantum information processing, *Phys. Rev. Lett.* **120**, 030502 (2018).

[26] H.-H. Lu, A. M. Weiner, P. Lougovski, and J. M. Lukens, Quantum information processing with frequency-comb

qudits, *IEEE Photon. Technol. Lett.* **31**, 1858 (2019).

[27] J. M. Lukens and P. Lougovski, Frequency-encoded photonic qubits for scalable quantum information processing, *Optica* **4**, 8 (2017).

[28] H.-H. Lu, J. M. Lukens, B. P. Williams, P. Imany, N. A. Peters, A. M. Weiner, and P. Lougovski, A controlled-not gate for frequency-bin qubits, *Npj Quantum Inf.* **5**, 1 (2019).

[29] H.-H. Lu, N. B. Lingaraju, D. E. Leaird, A. M. Weiner, and J. M. Lukens, High-dimensional discrete fourier transform gates with a quantum frequency processor, *Opt. Express* **30**, 10126 (2022).

[30] J. M. Lukens, H.-H. Lu, B. Qi, P. Lougovski, A. M. Weiner, and B. P. Williams, All-optical frequency processor for networking applications, *J. Light. Technol.* **38**, 1678 (2019).

[31] M. Liscidini and J. Sipe, Scalable and efficient source of entangled frequency bins, *Opt. Lett.* **44**, 2625 (2019).

[32] M. Clementi, F. A. Sabattoli, M. Borghi, L. Gianini, N. Tagliavacche, H. El Dirani, L. Youssef, N. Bergamasco, C. Petit-Etienne, E. Pargon, *et al.*, Programmable frequency-bin quantum states in a nano-engineered silicon device, *Nature Communications* **14**, 1 (2023).

[33] F. A. Sabattoli, L. Gianini, A. Simbula, M. Clementi, A. Fincato, F. Boeuf, M. Liscidini, M. Galli, and D. Bajoni, Silicon source of frequency-bin entangled photons, *Opt. Lett.* **47**, 6201 (2022).

[34] Y. Ding, D. Bacco, K. Dalgaard, X. Cai, X. Zhou, K. Rottwitt, and L. K. Oxenløwe, High-dimensional quantum key distribution based on multicore fiber using silicon photonic integrated circuits, *Npj Quantum Inf.* **3**, 1 (2017).

[35] See supplemental material at [url will be inserted by publisher], which contains refs. [45,46,47,48], for sample fabrication and geometry, experimental methods and numerical simulation of the impact of indistinguishability on density matrix reconstruction.

[36] L. Lu, L. Xia, Z. Chen, L. Chen, T. Yu, T. Tao, W. Ma, Y. Pan, X. Cai, Y. Lu, *et al.*, Three-dimensional entanglement on a silicon chip, *Npj Quantum Inf.* **6**, 1 (2020).

[37] M. G. Puigibert, G. Aguilar, Q. Zhou, F. Marsili, M. Shaw, V. Verma, S. Nam, D. Oblak, and W. Tittel, Heralded single photons based on spectral multiplexing and feed-forward control, *Phys. Rev. Lett.* **119**, 083601 (2017).

[38] T. Hiemstra, T. Parker, P. Humphreys, J. Tiedau, M. Beck, M. Karpiński, B. Smith, A. Eckstein, W. Kolthammer, and I. Walmsley, Pure single photons from scalable frequency multiplexing, *Phys. Rev. Appl.* **14**, 014052 (2020).

[39] P. Imany, N. B. Lingaraju, M. S. Alshaykh, D. E. Leaird, and A. M. Weiner, Probing quantum walks through coherent control of high-dimensionally entangled photons, *Sci. Adv.* **6**, eaba8066 (2020).

[40] S. Paesani, Y. Ding, R. Santagati, L. Chakhmakhchyan, C. Vigliar, K. Rottwitt, L. K. Oxenløwe, J. Wang, M. G. Thompson, and A. Laing, Generation and sampling of quantum states of light in a silicon chip, *Nat. Phys.* **15**, 925 (2019).

[41] L. S. Madsen, F. Laudenbach, M. F. Askarani, F. Rortais, T. Vincent, J. F. Bulmer, F. M. Miatto, L. Neuhaus, L. G. Helt, M. J. Collins, *et al.*, Quantum computational advantage with a programmable photonic processor, *Nature* **606**, 75 (2022).

[42] X. Gu, M. Erhard, A. Zeilinger, and M. Krenn, Quantum experiments and graphs ii: Quantum interference, computation, and state generation, *Proceedings of the National Academy of Sciences* **116**, 4147 (2019).

[43] A. Hochrainer, M. Lahiri, M. Erhard, M. Krenn, and A. Zeilinger, Quantum indistinguishability by path identity and with undetected photons, *RMP* **94**, 025007 (2022).

[44] C. Bellegarde, E. Pargon, C. Sciancalepore, C. Petit-Etienne, V. Hugues, D. Robin-Brosse, J.-M. Hartmann, and P. Lyan, Improvement of sidewall roughness of sub-micron soi waveguides by hydrogen plasma and annealing, *IEEE Photon. Technol. Lett.* **30**, 591 (2018).

[45] B. Birge, Psot-a particle swarm optimization toolbox for use with matlab, in *Proceedings of the 2003 IEEE Swarm Intelligence Symposium. SIS'03 (Cat. No. 03EX706)* (IEEE, 2003) pp. 182–186.

[46] S. Seshadri, N. Lingaraju, H.-H. Lu, P. Imany, D. E. Leaird, and A. M. Weiner, Nonlocal subpicosecond delay metrology using spectral quantum interference, arXiv preprint arXiv:2202.11816 (2022).

[47] L. G. Helt, Z. Yang, M. Liscidini, and J. E. Sipe, Spontaneous four-wave mixing in microring resonators, *Opt. Lett.* **35**, 3006 (2010).

# Supplemental material for A reconfigurable silicon photonics chip for the generation of frequency bin entangled qudits

Massimo Borghi,<sup>1,\*</sup> Noemi Tagliavacche,<sup>1</sup> Federico Andrea Sabattoli,<sup>1,†</sup> Houssein El Dirani,<sup>2,‡</sup> Laurene Youssef,<sup>3,§</sup> Camille Petit-Etienne,<sup>3</sup> Erwine Pargon,<sup>3</sup> J.E. Sipe,<sup>4</sup> Marco Liscidini,<sup>1</sup> Corrado Sciancalepore,<sup>2,¶</sup> Matteo Galli,<sup>1,\*\*</sup> and Daniele Bajoni<sup>5</sup>

<sup>1</sup>*Dipartimento di Fisica, Università di Pavia, Via Agostino Bassi 6, Pavia 27100, Italy*

<sup>2</sup>*Université Grenoble Alpes, CEA-Leti, Grenoble cedex 38054, France*

<sup>3</sup>*Univ. Grenoble Alpes, CNRS, CEA/LETI-Minatec, Grenoble INP, LTM, F-38054 Grenoble-France*

<sup>4</sup>*Department of Physics, University of Toronto, 60 St. George Street, Toronto, Ontario M5S 1A7, Canada*

<sup>5</sup>*Dipartimento di Ingegneria Industriale e dell'Informazione,  
Università di Pavia, Via Adolfo Ferrata 5, Pavia 27100, Italy*

(Dated: January 23, 2023)

## I. EXPERIMENTAL METHODS

### A. Sample fabrication

The device was fabricated at CEA-LETI (Grenoble) on a 200 nm silicon-on-insulator wafer manufactured by SOITEC (Bernin) with a 220 nm-thick device layer of crystalline silicon. Silicon structures are patterned by deep ultraviolet lithography with 120 nm resolution, followed by inductively coupled plasma etching (HBr/Cl<sub>2</sub>/He-O<sub>2</sub>, realized in collaboration with LTM (Laboratoire des Technologies de la Microélectronique)) and post-etch O<sub>2</sub> plasma for resist stripping. The sidewall roughness of the waveguides is reduced by hydrogen annealing [45]. After encapsulation resulting in a 900 nm-thick SiO<sub>2</sub> layer, 110 nm of titanium nitride (TiN) was deposited and patterned to create the thermal phase shifters. Aluminum copper (AlCu) was employed for the electrical pads. A deep etch comprising two different steps (C<sub>4</sub>F<sub>8</sub>/O<sub>2</sub>/CO/Ar plasma for the whole depth of SiO<sub>2</sub>, Bosch method to remove 150  $\mu$ m of the 725  $\mu$ m-thick Si substrate) was implemented to separate the sub-dice and to realize high quality end facets for edge coupling.

### B. Device geometry

The silicon waveguides have a cross section of 600 nm  $\times$  220 nm. The ring resonators have a radius of 22  $\mu$ m, and a coupling gap with the bus waveguide of 150 nm. The average separation between each resonator is 480  $\mu$ m. The three Mach-Zehnder interferometers are each made by two 50/50 splitters, which are realized using evanescent couplers (length 17.5  $\mu$ m, coupling gap 120 nm). The two arms have an equal length of 150  $\mu$ m, which coincides with that of the heater. The phase shifters PS1, PS2 and PS3 in Fig.1(a) of the main text are realized by heaters of length  $\sim$  120  $\mu$ m, which have a tuning efficiency of  $\sim$  15deg/mW.

### C. On chip state reconfiguration

Here we describe the step-by-step procedure that we implemented to generate the qutrit states  $|\Phi_2\rangle = (|11\rangle + |22\rangle + |33\rangle)/\sqrt{3}$  and  $|\Phi_3\rangle = (|11\rangle - |22\rangle - |33\rangle)/\sqrt{3}$ , and the two-ququart states  $|\Phi_5\rangle = (|00\rangle + |11\rangle + |22\rangle + |33\rangle)/2$  and  $|\Phi_6\rangle = (|00\rangle - |11\rangle - |22\rangle + |33\rangle)/2$ ; see the main text for a description of the bin labels. The procedure relies on the acquisition of two-photon interference fringes between adjacent pairs of frequency bins. These are obtained by projecting the signal and the idler photon onto  $\langle i|_{s(i)} + e^{i\theta_{s(i)}} \langle i+1|_{s(i)}$ , where  $i$  labels one of the frequency bins. Those projectors are realized by adjusting the RF power driving the phase modulators (PM) in order to equalize the

\* massimo.borghi@unipv.it

† Current address: Advanced Fiber Resources Milan S.r.L, via Fellini 4, 20097 San Donato Milanese (MI), Italy.

‡ Current address: LIGENTEC SA, 224 Bd John Kennedy, 91100 Corbeil-Essonnes, France.

§ Current address: IRCER, Centre Européen de la Céramique, 12 rue Atlantis, 87068 Limoges, France.

¶ Current address: SOITEC SA, Parc Technologique des Fontaines, Chemin des Franques, 38190 Bernin, France.

\*\* matteo.galli@unipv.it

intensities  $|J_{\pm 1}|$  of the first order sidebands to that of the baseband ( $|J_0|$ ); see below. The RF phase  $\theta_s = \theta_i = \bar{\theta}$  is varied to scan a two-photon interference fringe, which is proportional to  $\propto 1 + V \cos(2\bar{\theta})$  ( $V$  is the fringe visibility).

*Qutrit states:* for the state  $|\Phi_2\rangle$ , the relative phase between the biphoton emission from ring R1, R2, and R3 must be set equal. This is accomplished in two steps. First, we acquired a two-photon interference fringe by pumping only R1 and R2 (interference fringe 1-2). Second, a fringe is acquired by pumping only R2 and R3 (interference fringe 2-3). We then exploited the phase shifter PS1 (see Fig.1(a) in the main text) to align the two interference fringes. Note that one could have chosen the maximum of the fringe 1-2 as a reference, and used PS2 (or both PS1 and PS2) to align the maximum of two fringes. In the state  $|\Phi_3\rangle$ , the biphoton emission from R1 has a phase shift of  $\pi$  with respect to those from R2 and R3. In this case, we aligned the minimum of the fringe 1-2 to the maximum of the fringe 2-3.

*Ququart states:* for these states we acquired three interference curves, one for each pair of adjacent rings (R0-R1, R1-R2, and R2-R3). To generate the state  $|\Phi_5\rangle$ , the relative phase between the biphoton emission from all the four rings must be set equal. We then aligned the maxima of all the three interference curves through the phase shifters PS1, PS2, and PS3. To generate the state  $|\Phi_6\rangle$ , we must set a relative phase of  $\pi$  between the biphoton emission from R1 and R2 to those of R0 and R3. Using PS3 and PS2, we aligned the minimum of the fringe 2-3 to the maximum of the fringe 1-2. After that, using PS1 we aligned the minimum of the fringe 0-1 to the minimum of the fringe 2-3. In both the qutrit and the ququart cases, this procedure is repeated two times to mitigate the effect of thermal cross-talk between the heaters.

## II. DENSITY MATRIX RECONSTRUCTION

We implemented quantum state tomography to reconstruct the density matrix  $\rho$  of the state by performing a series of projective measurements. The probability  $p_q^{(j)}$  of getting one of the  $D^2$  ( $D$  is the dimension of each of the two qudits) measurement outcomes is given by

$$p_q^{(j)} = \text{Tr}(\rho \mathcal{P}_{jq}), \quad (1)$$

where  $\mathcal{P}_{jq}$  is a positive-operator-valued-measure (POVM), defined as  $\mathcal{P}_{jq} = U^\dagger(\gamma_j) |q\rangle \langle q| U(\gamma_j)$ . The operator  $U(\gamma_j) = U_s(P_s, \theta_s) \otimes U_i(P_i, \theta_i)$  describes the action of the electro-optic phase modulators (PMs) on the signal/idler photons, and  $|q\rangle$  indicates one of the  $D^2$  computational basis vectors. We use  $\gamma_j$  to label the  $j^{\text{th}}$  measurement setting, which comprises the RF power  $P_{s(i)}^{(\gamma_i)}$  and phase  $\theta_{s(i)}^{(\gamma_i)}$  of the signal and the idler PM. Equation 1 can be rewritten as

$$p_{mn} = \text{Tr}(\rho U^\dagger |mn\rangle \langle mn| U) = \langle mn| U \rho U^\dagger |mn\rangle, \quad (2)$$

where for simplicity  $U = U(\gamma_j)$ . For each measurement setting  $\gamma_j = (P_s, \theta_s, P_i, \theta_i)$ , we collected coincidence counts  $C_{mn}$  for all the possible  $\{(m, n) | m \in [0, \dots, D-1], n \in [0, D-1]\}$  ( $D$  is the qudit dimension) frequency bins combinations. The measurement settings used to reconstruct the density matrices are reported in Table I. The coincidence counts  $C_{mn}$  recorded in the experiment are related to the probabilities  $p_{mn}$  as

$$C_{mn} = R \cdot L_{mn} \cdot p_{mn}, \quad (3)$$

where  $R$  is the rate of photon pairs at the modulators and  $L_{mn}$  are (measured) the losses from the modulators to the detectors. We used the particle swarm optimization algorithm [46] to minimize the following cost function  $f_{\text{cost}}$

$$f_{\text{cost}} = \frac{1}{n_{\text{meas}}} \sum_{k=0}^{n_{\text{meas}}-1} \frac{(C_{\text{theo}}[k] - C_{\text{exp}}[k])^2}{2C_{\text{theo}}[k]}, \quad (4)$$

where  $n_{\text{meas}}$  is the number of measurements,  $C_{\text{exp}}$  is the vector containing the recorded coincidence measurements and  $C_{\text{theo}}$  is the vector of expected coincidence counts, which are calculated from a candidate density matrix  $\rho$  by using Eq.(3). The matrix  $\rho$  is parameterized by a vector of  $D^2$  real coefficients  $\mathbf{t}$  as

$$\rho(\mathbf{t}) = \frac{T(\mathbf{t})T^\dagger(\mathbf{t})}{\text{Tr}(T(\mathbf{t})T^\dagger(\mathbf{t}))}, \quad (5)$$

where  $T$  is a complex lower triangular matrix with real elements on the diagonal. The particle swarm algorithm minimizes  $f_{\text{cost}}$  in the parameter space spanned by  $(R, \mathbf{t})$ . We used  $N = 5$  measurement settings for  $D = 2$ , and  $N = 17$  for  $D = 3$  and  $D = 4$ , corresponding respectively to  $n_{\text{meas}} = 20 (D = 2)$ ,  $n_{\text{meas}} = 153 (D = 3)$  and  $n_{\text{meas}} = 272 (D = 4)$ . These are more than the  $D^4$  measurements required to unambiguously determine the density matrix, but the redundancy helped to speed up the convergence of the reconstruction algorithm.

Measurement setting ( $\gamma_j$ )	$P_s$ (dBm)	$\theta_s$ (rad)	$P_i$ (dBm)	$\theta_i$ (rad)
$\gamma_1$	0	0	0	0
$\gamma_2$	22.1	0	24.3	0
$\gamma_3$	22.1	$\frac{\pi}{2}$	24.3	$-\frac{\pi}{2}$
$\gamma_4$	22.1	0	0	0
$\gamma_5$	0	0	24.3	0

(a)

Measurement setting ( $\gamma_j$ )	$P_s$ (dBm)	$\theta_s$ (rad)	$P_i$ (dBm)	$\theta_i$ (rad)
$\gamma_1$	22.1	0	24.3	0
$\gamma_2$	22.1	0	24.3	$\frac{4\pi}{3}$
$\gamma_3$	22.1	0	24.3	$-\frac{4\pi}{3}$
$\gamma_4$	22.1	0	24.3	$\frac{2\pi}{3}$
$\gamma_5$	22.1	$\frac{4\pi}{3}$	24.3	0
$\gamma_6$	22.1	$\frac{4\pi}{3}$	24.3	$\frac{4\pi}{3}$
$\gamma_7$	22.1	$\frac{4\pi}{3}$	24.3	$-\frac{4\pi}{3}$
$\gamma_8$	22.1	$\frac{4\pi}{3}$	24.3	$\frac{2\pi}{3}$
$\gamma_9$	22.1	$-\frac{4\pi}{3}$	24.3	0
$\gamma_{10}$	22.1	$-\frac{4\pi}{3}$	24.3	$\frac{4\pi}{3}$
$\gamma_{11}$	22.1	$-\frac{4\pi}{3}$	24.3	$-\frac{4\pi}{3}$
$\gamma_{12}$	22.1	$-\frac{4\pi}{3}$	24.3	$\frac{2\pi}{3}$
$\gamma_{13}$	22.1	$\frac{2\pi}{3}$	24.3	0
$\gamma_{14}$	22.1	$\frac{2\pi}{3}$	24.3	$\frac{4\pi}{3}$
$\gamma_{15}$	22.1	$\frac{2\pi}{3}$	24.3	$-\frac{4\pi}{3}$
$\gamma_{16}$	22.1	$\frac{2\pi}{3}$	24.3	$\frac{2\pi}{3}$
$\gamma_{17}$	0	0	0	0

(b)

TABLE I: Signal and idler measurement settings  $\gamma_j$  used to perform quantum state tomography on qubit (a) and qutrit-ququart (b) states. We report the RF powers  $P_s$ ,  $P_i$  and the phases  $\theta_s$ ,  $\theta_i$  of the signals driving the signal and the idler PM. The values  $P_s = 22.1$  dBm and  $P_i = 24.3$  dBm correspond to a modulation index of  $\beta \sim 1.434$ , for which the intensities of the first order sidebands  $J_{\pm 1}$  are equal to that of the baseband  $J_0$  (the fact that  $P_s < P_i$  is due to the higher modulation efficiency of the signal PM)

### A. Impact of source indistinguishability on the reconstruction of the density matrix

The density matrix reconstruction is done through a series of projective measurements whose probability outcomes  $p_{mn}$  on the bin combination  $\{(m, n) | m \in [0, \dots, D-1], n \in [0, D-1]\}$  ( $D$  is the qudit dimension) are given by Eq.(2). The two-photon state  $|\Psi\rangle$  generated by our device is:

$$|\Psi\rangle = \sum_{k=0}^{D-1} \alpha_k \int \phi_k(\omega_{k_s} + \Omega_1, \omega_{k_i} + \Omega_2) |\omega_{k_s} + \Omega_1, \omega_{k_i} + \Omega_2\rangle d\Omega_1 d\Omega_2, \quad (6)$$

where  $\phi_k$  is the joint spectral amplitude of the  $k^{\text{th}}$  ring resonator [47], which generates photon pairs in the signal/idler bins  $|k\rangle_i |k\rangle_s$ , and  $\{\alpha\}_{k=0,\dots,D-1}$  is a list of complex coefficients such that  $\sum_k |\alpha_k|^2 = 1$ . The resonance frequency associated to the signal(idler) bin  $k$  (see Fig.1(c) in the main text) is  $\omega_{k_s(i)}$ . The density matrix  $\rho$  then writes

$$\rho = \sum_{\{k,k'\}=0}^{D-1} \int \alpha_k \alpha_{k'}^* \phi_k(\omega_{k_s} + \Omega_1, \omega_{k_i} + \Omega_2) \phi_{k'}^*(\omega_{k'_s} + \Omega'_1, \omega_{k'_i} + \Omega'_2) |\omega_{k_s} + \Omega_1, \omega_{k_i} + \Omega_2\rangle \langle \omega_{k'_i} + \Omega'_2, \omega_{k'_s} + \Omega'_1| d\Omega_1 d\Omega'_1 d\Omega_2 d\Omega'_2. \quad (7)$$

Under the action of the PMs, the density matrix in Eq.(7) evolves as  $\rho \rightarrow U\rho U^\dagger$ , where  $U = U_i \otimes U_s$  transforms the signal/idler annihilation operator  $a$  as

$$U_{s(i)} a_m(\omega_{m_{s(i)}} + \omega) U_{s(i)}^\dagger = \sum_{r=-\infty}^{+\infty} V_{mr}^{s(i)} a(\omega_{r_{s(i)}} + \omega). \quad (8)$$

The coefficients  $V_{mr}^{s(i)}$  are related to the Bessel functions of first kind  $J_{m-r}$ , of order  $r-m$ , as

$$V_{mr}^{s(i)} = J_{r-m}(\beta^{(\gamma_i)}) e^{i(r-m)\theta_{s(i)}^{(\gamma_i)}}, \quad (9)$$

which depend on both the strength of the modulation index  $\beta^{(\gamma_i)}$  and on the phase  $\theta_{s(i)}^{(\gamma_i)}$  of the RF signal applied to the phase modulators in the measurement setting  $\gamma_i$  [22, 48]. After the transformation described by  $U$ , coincidences between the signal and the idler photon are collected in the bin combinations  $(m, n)$ , which are selected by using two fiber-Bragg-gratings (FBG). The center frequency of the stop band of the signal and the idler FBGs are set to be respectively  $\omega_{n_s}$  and  $\omega_{m_i}$ . With good approximation, we can model the transfer function of the reflection port of the FBG (i.e., the one connected to the single photon detector) as a box centered at  $\omega_{n(m)_{s(i)}}$  and with a bandwidth of  $2\Delta$ . Since the frequencies within the stop band are not resolved, the action of the FBG is described by the operator  $P_{mn} = P_m^{(i)} \otimes P_n^{(s)}$ , where

$$P_q^{(i,s)} = \int_{-\Delta}^{\Delta} |\omega_{q_{i(s)}} + \omega\rangle \langle \omega + \omega_{q_{i(s)}}| d\omega. \quad (10)$$

Using Eqs.(2,10) we obtain

$$p_{mn} = \int_{-\Delta}^{\Delta} \int_{-\Delta}^{\Delta} \langle \omega_{m_i} + \omega, \omega_{n_s} + \omega' | U\rho U^\dagger | \omega_{n_s} + \omega', \omega_{m_i} + \omega \rangle d\omega d\omega'. \quad (11)$$

We now use Eq.(8) to write

$$U^\dagger |\omega_{n_s} + \omega', \omega_{m_i} + \omega\rangle = \sum_{\{r_i, q_s\}=-\infty}^{+\infty} (V_{rm}^i V_{qn}^s)^* |\omega_{q_s} + \omega', \omega_{r_i} + \omega\rangle \quad (12)$$

which substituted in Eq.(11) gives

$$p_{mn} = \sum_{\{k,k'\}} \sum_{\{r_i, q_s, r'_i, q'_s\}} \int \phi_k \phi_{k'}^* \langle \omega_{r'_i} + \omega, \omega_{q'_s} + \omega' | \omega_{k_s} + \Omega_1, \omega_{k_i} + \Omega_2 \rangle \langle \omega_{k'_i} + \Omega'_2, \omega_{k'_s} + \Omega'_1 | \omega_{q_s} + \omega', \omega_{r_i} + \omega \rangle \times \quad (13)$$

$$\alpha_k \alpha_{k'}^* V_{mr'}^i V_{nq'}^s (V_{rm}^i V_{qn}^s)^* d\omega d\omega' d\Omega_1 d\Omega_2 d\Omega'_1 d\Omega'_2 \quad (14)$$

The different frequency bins do not overlap, and they are fully contained within bandwidth  $2\Delta$  of the FBGs, which allows us to write

$$\begin{aligned} \langle \omega_{r'_i} + \omega, \omega_{q'_s} + \omega' | \omega_{k_s} + \Omega_1, \omega_{k_i} + \Omega_2 \rangle &= \delta(\omega' - \Omega_1) \delta(\omega - \Omega_2) \delta_{r'_i, k_i} \delta_{q'_s, k_s}, \\ \langle \omega_{k'_i} + \Omega'_2, \omega_{k'_s} + \Omega'_1 | \omega_{q_s} + \omega', \omega_{r_i} + \omega \rangle &= \delta(\omega' - \Omega'_1) \delta(\omega - \Omega'_2) \delta_{r_i, k'_i} \delta_{q_s, k'_s}. \end{aligned}$$

By performing the integrals over  $\Omega_1, \Omega_2, \Omega'_1, \Omega'_2$ , and the sums over  $\{r_i, r'_i, q_s, q'_s\}$  we obtain

$$p_{mn} = \sum_{\{k,k'\}} V_{mk_i}^i V_{nk_s}^s (V_{k'_i m}^i V_{k'_s n}^s)^* \alpha_k \alpha_{k'}^* \int \phi_k(\omega_{k_s} + \omega', \omega_{k_i} + \omega) \phi_{k'}^*(\omega_{k'_s} + \omega', \omega_{k'_i} + \omega) d\omega d\omega'. \quad (15)$$

The overlap integral between the joint spectral amplitude  $\phi_k$  and  $\phi_{k'}$  on the right hand side of Eq.(15) is the indistinguishability  $I_{kk'}$  between source  $k$  and  $k'$ , i.e.

$$I_{kk'} = \int \phi_k(\omega_{k_s} + \omega', \omega_{k_i} + \omega) \phi_{k'}^*(\omega_{k'_s} + \omega', \omega_{k'_i} + \omega) d\omega d\omega'. \quad (16)$$

The final expression for the probability  $p_{mn}$  of measuring a coincidence in the bin combination  $(m, n)$  after that the transformation  $U$  has been applied is then

$$p_{mn} = \sum_{\{k, k'\}} \alpha_k \alpha_k'^* I_{kk'} V_{mk_i}^i V_{nk_s}^s (V_{k'_i m}^i V_{k'_s n}^s)^* \quad (17)$$

We now demonstrate that the same probability outcome in Eq.(17) can be obtained from a density matrix  $\rho'$  with entries  $\rho'_{ij,kl} = \langle ij | \rho' | kl \rangle = I_{ik} \alpha_i \alpha_k^* \delta_{ij} \delta_{kl}$ . The basis state  $|ij\rangle$  describes a signal and an idler photon respectively in the frequency bins  $|i\rangle$  and  $|j\rangle$ . Compared to the definition of  $\rho$  in Eq.(7), the density matrix  $\rho'$  neglects any intra-bin frequency correlation in favor of a simpler description of the state, in which the frequency distribution is collapsed to a single label index. Note that in the limit  $I_{ij} \rightarrow 1$ , i.e. when all the sources are perfectly indistinguishable, we have that  $\rho' \rightarrow |\Phi\rangle\langle\Phi|$ , where  $|\Phi\rangle = \sum_{k=0}^{D-1} \alpha_k |kk\rangle$ . When  $|\alpha_k| = D^{-1/2}$ ,  $|\Phi\rangle$  describes a maximally entangled Bell state. We can use Eq.(2) to calculate the probability of measuring a coincidence over the bin combination  $(m, n)$  after that the transformation  $U$  has been applied, which gives

$$\begin{aligned} p_{mn} &= \langle mn | U \rho' U^\dagger | mn \rangle \\ &= \sum_{i,j} \alpha_i \alpha_j^* I_{ij} \langle mn | U | ii \rangle \langle jj | U^\dagger | mn \rangle \\ &= \sum_{i,j} \sum_{p,q,r,s} (V_{pm}^i V_{qn}^s)^* V_{mr}^i V_{ns}^s \alpha_i \alpha_j^* I_{ij} \langle rs | ii \rangle \langle jj | pq \rangle \\ &= \sum_{ij} \alpha_i \alpha_j^* I_{ij} (V_{jm}^i V_{jn}^s)^* V_{mi}^i V_{ni}^s, \end{aligned} \quad (18)$$

which coincides with the expression in Eq.(17). In the density matrix reconstruction algorithm described in section II, we neglect the intra-bin frequency correlations and represent  $\rho$  on the  $D^2$ -dimensional basis  $|mn\rangle$ , where  $\{(m, n) | m \in [0,..,D-1], n \in [0, D-1]\}$ . By construction, the algorithm does not return the density matrix  $\rho$  in Eq.(7), but gives the maximum likelihood estimation of  $\rho'$ .

## B. Impact of source indistinguishability on the purity and the fidelity of the reconstructed density matrix

The indistinguishability between all the sources determines the maximum amount of purity and fidelity with the target states that can be achieved by the reconstructed density matrices. We investigated how these quantities vary with the indistinguishability  $I_{jk}$ , which appear in the density matrix as  $\rho'_{ij,kl} = \langle ij | \rho' | kl \rangle = I_{ik} \alpha_i \alpha_k^* \delta_{ij} \delta_{kl}$ . For simplicity, we assumed that all the sources have an equal pair-wise indistinguishability, i.e.  $I_{jk} = I$ . Note that in the limit  $I \rightarrow 1$ , i.e. when all the sources are perfectly indistinguishable, we have that  $\rho' \rightarrow |\Phi\rangle\langle\Phi|$ , where  $|\Phi\rangle = \sum_{k=0}^{D-1} \alpha_k |kk\rangle$ . When  $|\alpha_k| = D^{-1/2}$ ,  $|\Phi\rangle$  describes a maximally entangled Bell state. In our analysis, we set  $|\alpha_k| = D^{-1/2}$ , and we calculated the purity  $\mathcal{P}$  and the fidelity  $\mathcal{F}$  with the maximally entangled Bell state  $|\Phi\rangle$  as a function of  $I$  for  $D = 2, 3, 4$ . The results are shown in Fig.1. In the experiment, we measured an average indistinguishability of  $\bar{I} = 0.87(7)$ . This value is marked in Fig. 1 with a dashed line, while the gray area encloses the confidence bounds. The range of values assumed by the purity and the fidelity over that region are reported in Table II. These values are compared with the purities  $\mathcal{P}$  and the fidelities  $\mathcal{F}$  extracted from the reconstructed density matrices in the experiment. In Table II, we reported these values for the target states  $|\Phi_1\rangle$  (qubit),  $|\Phi_2\rangle$  (qutrit), and  $|\Phi_5\rangle$  (ququart) (see definitions in Table 1 of the main text). Except for the purity of the qubit, which is slightly higher in the experiment than in the simulation, all the values lie in the confidence intervals predicted by the simulation.

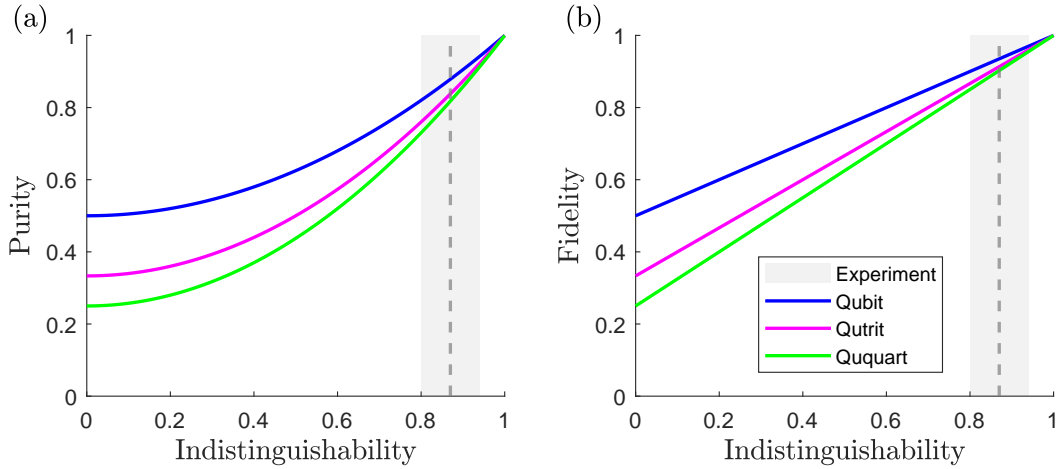


FIG. 1: Simulated purity (a) and fidelity (b) with maximally entangled Bell states  $|\Phi\rangle = \sum_{k=0}^{D-1} |kk\rangle$  of the density matrix  $\rho'$  as a function of the indistinguishability  $I$ . The dashed line marks the average value of indistinguishability  $\bar{I} = 0.87(7)$  obtained in the experiment. The grey region represents the confidence bound of  $\bar{I}$ .

State	Simulated purity	Simulated fidelity	Experimental purity	Experimental fidelity
Qubit	[81 – 94]	[89 – 96]	94.63(4)	95.0(2)
Qutrit	[76 – 92]	[86 – 96]	78.3(5)	86.2(3)
Ququart	[73 – 91]	[84 – 95]	74.4(4)	84.5(2)

TABLE II: Measured and simulated purities and fidelities (percentage) for the qubit, qutrit and quaquart states. The interval bounds indicate the lower and the upper value of the purity and the fidelity over the confidence bounds of the indistinguishability  $\bar{I}$ .

---

[45] C. Bellegarde, E. Pargon, C. Sciancalepore, C. Petit-Etienne, V. Hugues, D. Robin-Brosse, J.-M. Hartmann, and P. Lyan, Improvement of sidewall roughness of submicron soi waveguides by hydrogen plasma and annealing, *IEEE Photon. Technol. Lett.* **30**, 591 (2018).

[46] B. Birge, Psot-a particle swarm optimization toolbox for use with matlab, in *Proceedings of the 2003 IEEE Swarm Intelligence Symposium. SIS'03 (Cat. No. 03EX706)* (IEEE, 2003) pp. 182–186.

[47] L. G. Helt, Z. Yang, M. Liscidini, and J. E. Sipe, Spontaneous four-wave mixing in microring resonators, *Opt. Lett.* **35**, 3006 (2010).

[22] H.-H. Lu, K. V. Myilswamy, R. S. Bennink, S. Seshadri, M. S. Alshaykh, J. Liu, T. J. Kippenberg, D. E. Leaird, A. M. Weiner, and J. M. Lukens, Bayesian tomography of high-dimensional on-chip biphoton frequency combs with randomized measurements, *Nat. Commun.* **13**, 1 (2022).

[48] S. Seshadri, N. Lingaraju, H.-H. Lu, P. Imany, D. E. Leaird, and A. M. Weiner, Nonlocal subpicosecond delay metrology using spectral quantum interference, arXiv preprint arXiv:2202.11816 (2022).